Chemical Science

ROYAL SOCIETY OF CHEMISTRY

EDGE ARTICLE

View Article Online
View Journal | View Issue

Cite this: *Chem. Sci.*, 2025, **16**, 21932

All publication charges for this article have been paid for by the Royal Society of Chemistry

Received 9th July 2025
Accepted 14th October 2025

DOI: 10.1039/d5sc05078b

rsc.li/chemical-science

Brønsted acid-promoted ethylene dimerization to 1-butene over Ni-containing zeolite catalysts

Li Wang,[a] Yuwen Ni,[a] Jingyao Yang,[a] Guangjun Wu,[a] Yuchao Chai *[ab] and Landong Li[ab]

Ethylene dimerization is a critical industrial process traditionally catalyzed by homogeneous systems employing cocatalysts or solvents. Although heterogeneous catalysts show potential to circumvent these limitations, they often exhibit low activity and limited selectivity toward 1-butene. In this work, a transition-metal-confined FAU zeolite catalyst featuring precisely defined, coordinatively unsaturated Ni sites and abundant acidic functionalities, is explored for the reaction. This unique catalyst, denoted as H–Ni@Y, demonstrates remarkable ethylene dimerization performance without the need for cocatalysts or additive activators. In a fixed-bed reactor, an exceptional 1-butene formation rate of 4.28×10^5 h^{-1} and high 1-butene selectivity of 83.6% can be achieved with H–Ni@Y catalyst. Comprehensive characterization results and DFT calculations elucidate the significant influence of Brønsted acidity on the catalytic performance, revealing the *in situ*-generated Ni–alkyl species as the active sites. The reaction proceeds *via* the Cossee–Arlman mechanism, facilitated by dynamic proton transfer processes. These findings provide valuable insights into the rational design of heterogeneous catalysts for industrially relevant ethylene dimerization.

1 Introduction

1-Butene, an essential petroleum-derived chemical within the linear α-olefins family, is extensively utilized as an intermediate in the manufacture of linear low-density and high-density polyethylene.[1,2] Ethylene dimerization remains the primary industrial route for synthesizing 1-butene, exemplified by commercial processes such as the IFP-SABIC (Ti-based Alphabutol), Phillips (Ni-based) and DOW (triethyl aluminum-based) technologies.[3] Although homogeneous catalysts employed in these processes have achieved high catalytic activity, they exhibit notable drawbacks, including difficult product separation, complex catalyst recycling, solvent dependence, and, more significantly, the necessity for expensive alkylaluminum cocatalysts like methylaluminoxane (MAO) or trimethylaluminum.[4–6] Driven by green chemistry principles (*e.g.*, cocatalyst/solvent-free operation), heterogeneous catalysts have gained attention as viable alternatives. Prominent examples include (i) metal–organic frameworks (MOFs),[7] (ii) oxide-supported immobilized metal complexes[8] and (iii) transition metal containing solid acid material such as zeolites.[9] Nevertheless, categories (i) and (ii) generally require cocatalysts and involve intricate preparation and regeneration procedures, thereby limiting their large-scale implementation.[10,11]

Zeolites, as the classic solid acids widely employed industrially, can effectively host metal ions within their matrix, creating coordinated metal centers active for ethylene dimerization.[12–15] Ni-modified zeolites containing acid sites have exhibited significant potential for ethylene dimerization.[16–18] However, current Ni-zeolite catalysts generally display inferior 1-butene selectivity and substantially lower activity compared to optimized homogeneous Ni catalysts, restricting their practical use. In our recent work,[19] a simple two-step ion-exchange strategy was developed to synthesize Ni–Mg–Y zeolites as a high-performance catalyst in ethylene dimerization without any additives, achieving state-of-the-art performance among heterogeneous systems. This method strategically employed alkali metal ions (Mg^{2+}) at Site **I**, promoting Ni^{2+} incorporation at Site **II** (Scheme S1), thus optimizing the catalytic coordination environment. The dynamic hydrogen transfer between ethylene/alkyl intermediates and zeolite framework significantly contributes to catalytic activity, effectively mimicking the role of cocatalysts in homogeneous systems. Hypothetically, zeolites abundant in Brønsted acid sites (*e.g.*, Ni–H–Y) could enhance hydrogen transfer processes and ethylene dimerization efficacy relative to Ni–Mg–Y; however, the H^+ exchange does not similarly position Ni^{2+} at Site **II** using this method.

Herein, a hydrothermal synthesis route was employed to prepare Na–Ni@Y zeolites with Ni positioned exclusively at Site

[a]*Key Laboratory of Advanced Energy Materials Chemistry of Ministry of Education, College of Chemistry, Nankai University, Tianjin 300071, P.R. China. E-mail: cyc@nankai.edu.cn*

[b]*Frontiers Science Center for New Organic Matter, Nankai University, Tianjin 300071, P.R. China*

II, followed by NH^{4+} ion exchange to yield H–Ni@Y zeolites enriched in Brønsted acid sites. The resultant H–Ni@Y catalyst demonstrated superior catalytic performance, achieving a turnover frequency (TOF) of 4.28×10^5 h^{-1} and 83.6% selectivity toward 1-butene, surpassing Ni–Mg–Y. Detailed spectroscopic characterization results and DFT calculations on the well-defined H–Ni@Y catalyst provided insights into the reaction mechanism, clearly establishing the reaction pathway for additive-free ethylene dimerization to 1-butene.

2 Results and discussion

2.1 Characterization of H–Ni@Y

A typical ligand-protected hydrothermal method was employed to encapsulate Ni complexes within the faujasite (FAU) zeolite framework, followed by introducing additional acidic sites through a simple post ion exchange process (Fig. 1a). Coordinated Ni species were initially confined within the sodalite (SOD) cages, with subsequent calcination inducing thermally driven migration of Ni ions to Site **II** within the six-membered rings of the SOD cages, enabling selective stabilization at their most energetically favorable sites.[20,21] The well-defined Ni sites in H–Ni@Y, achieved *via in situ* synthesis, are essential for elucidating the reaction mechanism and controlling product selectivity, a level of precision unattainable through conventional ion exchange methods. Ion exchange of H^+ cations in the FAU framework with ammonium acetate (NH_4Ac) solution resulted in NH_4–Ni@Y, yielding protonated H–Ni@Y upon calcination in air.[22] X-ray diffraction (XRD, Fig. S1), scanning electron microscopy (SEM, Fig. 1b and S2), and high-resolution transmission electron microscopy (HR-TEM, Fig. 1c) confirmed the successful synthesis of H–Ni@Y with characteristic FAU topology. Energy-dispersive X-ray spectroscopy (EDS, Fig. 1d), mapping scans (Fig. 1e), and line scans (Fig. 1f and g) revealed the uniform dispersion of isolated Ni species within the H–Ni@Y zeolite. The Ni loading in H–Ni@Y was determined to be 2.96% (XRF, Table S1). H–Ni@Y exhibited typical microporous characteristics, as evidenced by type **I** adsorption isotherms, total surface area of 415.8 cm^2 g^{-1} (Fig. S3 and Table S2) and an average pore diameter of approximately ~7 Å (Fig. S4).[23] Thermogravimetric analysis coupled with differential scanning calorimetry (TG-DSC, Fig. S5) of H–Ni@Y in the flowing air revealed the complete removal of organic ligands at below 600 K.

Notably, H–Ni@Y presented a characteristic hydrogen consumption peak at about 1010 K in the hydrogen temperature-programmed reduction profiles (H_2-TPR, Fig. S6), markedly different from the those of H–Ni–Y synthesized by conventional ion exchange and Ni/HY prepared by impregnation, indicating the uniform distribution and superior stability of Ni ions in H–Ni@Y.[21] The integrated differential phase contrast scanning transmission electron microscopy (iDPC-STEM) images (Fig. 1h) of H–Ni@Y provided direct evidence for the uniformly dispersion of isolated Ni within the FAU matrix, showing the atomically dispersed Ni species positioned at the interfaces between the sodalite cages and supercages (Site **II**), which was consistent with the subsequent X-ray absorption spectroscopy (XAS) results.

The Ni coordination environment significantly influenced the catalytic performance. The X-ray photoelectron spectroscopy (XPS, Fig. S7) confirmed the chemical composition and electronic state of Ni species in Ni-containing zeolites, revealing a Ni $2p_{3/2}$ binding energy value of 856.4 eV for H–Ni@Y, higher than that of NiO according to literature.[24] It indicated the existing states of Ni^{2+} species and the electron transfer from Ni to the zeolite framework.[25] X-ray absorption spectroscopy (XAS), including X-ray absorption near-edge structure (XANES) and extended X-ray absorption fine structure (EXAFS), provided detailed insights into the electronic structure and local coordination environment of Ni. The XANES spectrum of H–Ni@Y displayed a white line peak near NiO (Fig. 2a), confirming the +2 oxidation state and interactions between Ni and framework oxygen atoms, consistent with XPS results. The pre-edge peaks (8333–8335 eV) for Na–Ni@Y (Fig. S8) and H–Ni@Y (Fig. 2a) were notably more intense compared to Ni foil and NiO, further supporting Ni^{2+} coordination.[26] Fourier-transform (FT) k^3-weighted *R*-space EXAFS spectrum of H–Ni@Y (Fig. 2b and Table S3) prominently featured a peak at 2.06 Å contributed to the first shell of Ni–O/C scattering path, with an average coordination number of approximately 3.8 (Fig. 2e and Table S3).[21,27] A secondary peak observed near 2.96 Å can be attributed to second-shell interactions involving Si or Al atoms, indicating the Ni–O–Si or Ni–O–Al interactions (Fig. 2c–**e** and Table S3). Analogously, the wavelet-transformed (WT) EXAFS oscillations of Ni foil, NiO, and H–Ni@Y (Fig. 2f–**h**) provided further information about the *R*- and *k*-space resolutions of the scattering atoms, the WT EXAFS counter plots exhibited an intensity maximum at about 4.5 $Å^{-1}$ in *k*-space, according to the Ni–O path, without Ni–Ni paths detected. Collectively, these findings, along with H_2-TPR data, conclusively indicate the formation of four-coordinated Ni^{2+} species confined within the FAU zeolite matrix.

The nature and concentration of acidic sites may significantly influence the catalytic performance in ethylene dimerization. Moderate-strength Brønsted acid sites in zeolites typically favor selective linear product formation, such as 1-butene, while stronger Brønsted sites may induce undesired cracking or isomerization side reactions due to their higher reactivity.[28] The combination of NH_3 temperature-programmed desorption (NH_3-TPD, Fig. 3a, b, S9, S10 and Table S4) and pyridine-adsorbed infrared spectroscopy (Py-IR, Fig. 3c, d and S11–S16) provides comprehensive characterization of zeolite acidity. NH_3-TPD offers reliable insights into both the concentration and strength distribution of acid sites. Following ion exchange with NH_4OAc solution, the acid strength of H–Ni@Y notably increased. The desorption peaks ~440 K, ~550 K, ~720 K and ~950 K were attributed to weak acid sites, medium acid sites and strong acid sites, respectively.[29] It was demonstrated that acid strength enhancement positively correlated with ethylene dimerization activity.[30,31] The higher NH_3 desorption amount observed for H–Ni@Y compared to Na–Ni@Y (Fig. 3a and Table S4) indicated additional acidic sites introduced *via* NH_4Ac ion exchange and subsequent calcination. H–Ni@Y exhibited the highest total acid content among all samples (Table S4), with its medium and strong acid levels also

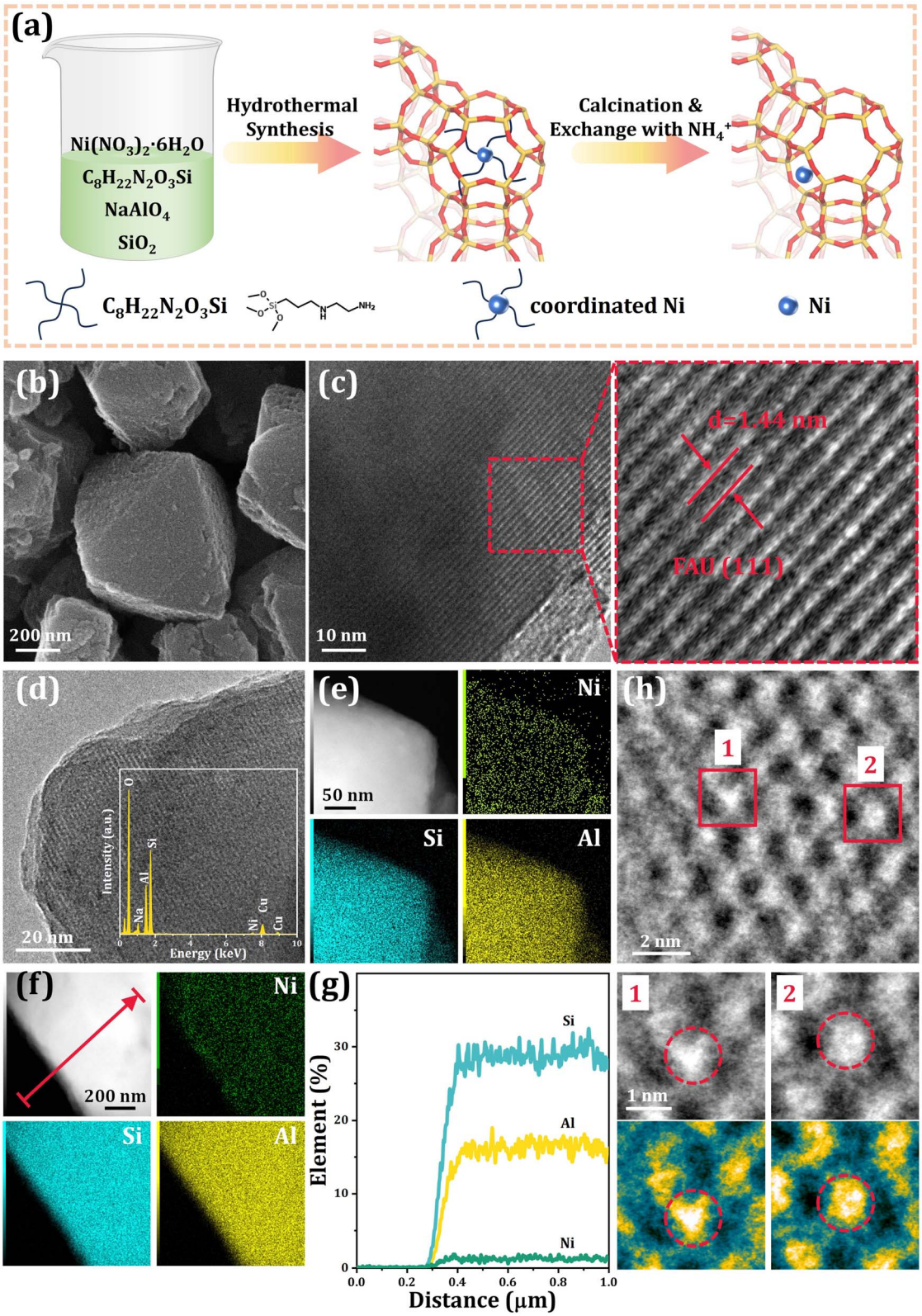

Fig. 1 Synthesis and characterization of H–Ni@Y. (a) Fabrication process of FAU zeolites and schematic of Ni occupancy in H–Ni@Y; (b) SEM image, (c) HR-TEM and enlarged view of selected region, (d) EDS analysis (the insert was the element dispersive spectrum), (e) EDS mappings, (f and g) line scan (the red arrow indicated the line scan position), and (h) iDPC-STEM images of samples.

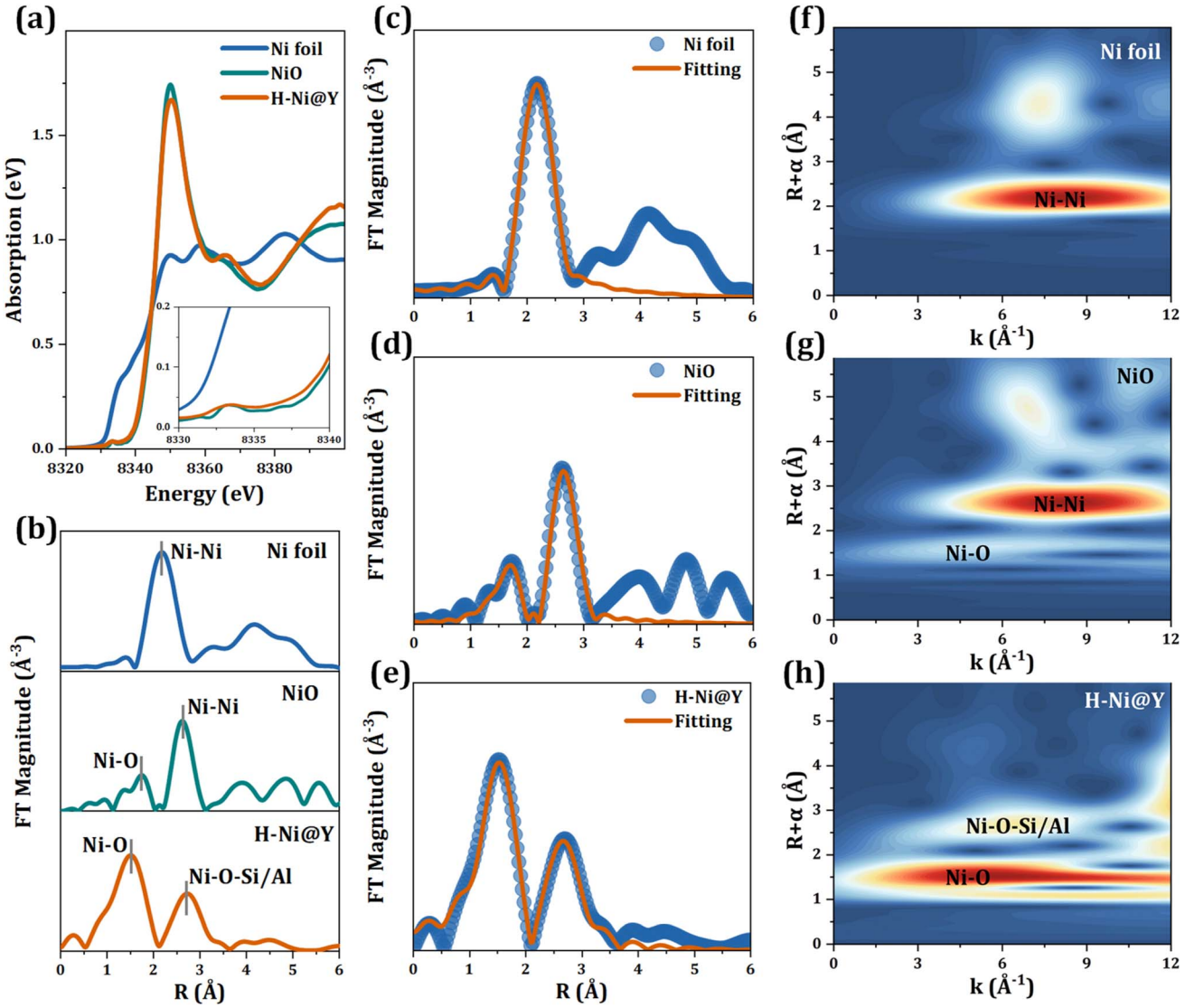

Fig. 2 XAS characterization of H–Ni@Y sample. X-ray absorption spectroscopy analyses of H–Ni@Y zeolite. (a) Ni K-edge XANES spectra of H–Ni@Y, NiO, and Ni foil; (b) FT EXAFS spectra of H–Ni@Y, NiO, and Ni foil; FT EXAFS fitting spectra of (c) Ni foil, (d) NiO, and (e) H–Ni@Y at the *R*-space; and WT EXAFS spectra of (f) Ni foil, (g) NiO, and (h) H–Ni@Y.

surpassing those of other catalysts. Comparison between H–Ni@Y and pristine H–Y confirms that Ni^{2+} incorporation introduces additional Lewis acid sites (Fig. S10). These Ni-derived Lewis sites may participate in hydrogen transfer, complementing the Brønsted acid sites. However, control experiments clearly indicate that Brønsted acidity remains the dominant factor governing hydrogen-transfer steps (Fig. S44).

2.2 Ethylene selective dimerization to 1-butene over H–Ni@Y

The catalytic performance of H–Ni@Y and various control catalysts was systematically evaluated in a continuous-flow fixed-bed reactor. Reaction parameters, including ethylene pressure, gas hourly space velocity (GHSV), NH_4OAc solution concentration, and ammonium salt selection were carefully optimized, as detailed in Fig. S17–S22. Comparative ethylene dimerization experiments using Na–Ni@Y (Fig. 4a) and H–Ni@Y (Fig. 4b) catalysts were performed under optimized reaction conditions within the temperature range of 298 to 393 K. Notably, the H–Ni@Y catalyst exhibited superior catalytic activity, achieving remarkable selectivity towards 1-butene (83.6%) along with an exceptionally high turnover frequency (TOF) of 4.28×10^5 h^{-1} at 333 K, significantly outperforming the Na–Ni@Y catalyst. Post-reaction characterizations employing X-ray diffraction (XRD, Fig. S23), scanning electron microscopy (SEM, Fig. S24), BET surface area measurements (Fig. S25, S26 and Table S2), thermogravimetric differential scanning calorimetry (TG-DSC, Fig. S27), and X-ray photoelectron spectroscopy (XPS, Fig. S28) consistently confirmed the robust structural stability and the preservation of the coordination environment of Ni within the zeolite matrix. The acidity of used H–Ni@Y declined significantly as shown in Py-IR

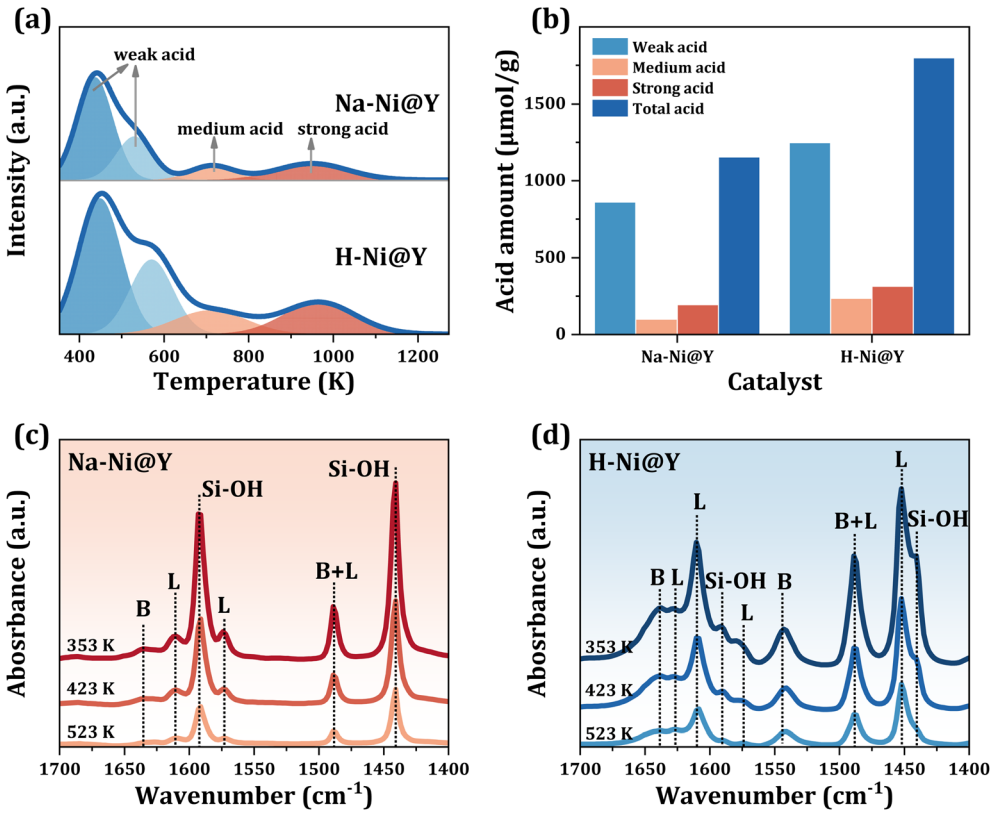

Fig. 3 Acidity characterization. (a) NH_3-TPD profiles of Na–Ni@Y and H–Ni@Y; (b) the distribution of acidity in the Na–Ni@Y and H–Ni@Y; the Py-IR spectra of (c) Na–Ni@Y and (d) H–Ni@Y.

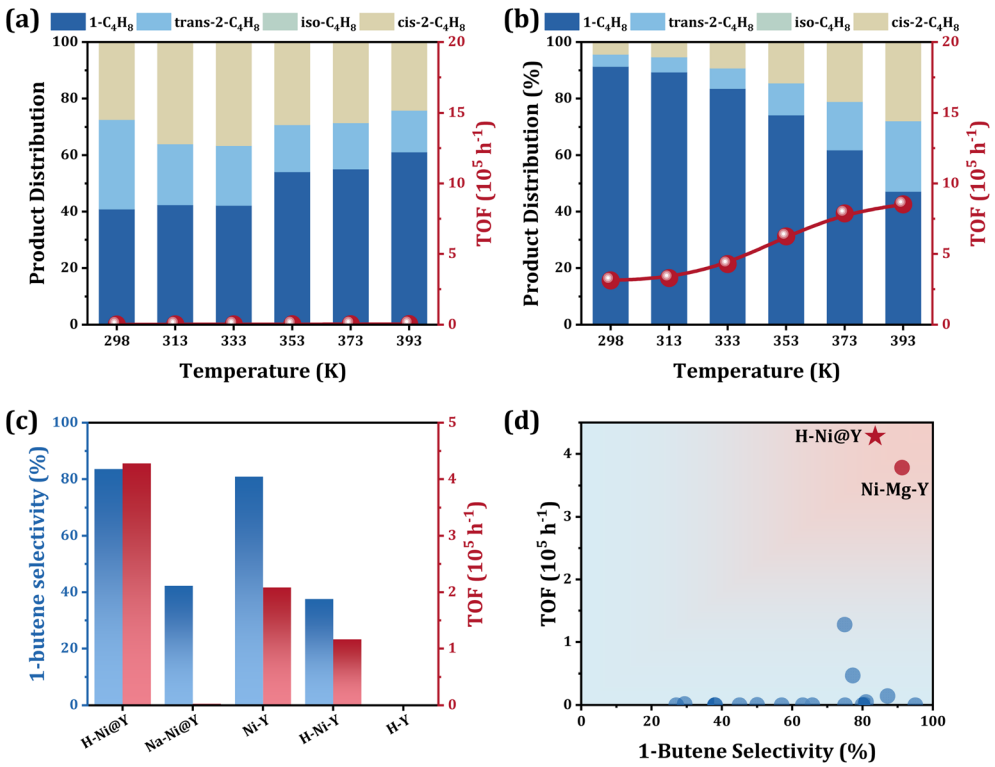

Fig. 4 Catalytic performance in ethylene dimerization. Ethylene dimerization performance over (a) Na–Ni@Y, (b) H–Ni@Y and (c) Ni-containing control samples. Reaction condition: 0.1 g catalyst, 3.0 MPa pure C_2H_4, GHSV = 18 000 h^{-1}. (d) Literature survey of Ni-containing zeolite catalysts for ethylene dimerization in terms of 1-butene selectivity and ethylene dimerization rates.

(Fig. S29) and NH_3-TPD (Fig. S30 and Table S4). The apparent decrease in acidity is fully reversible and arises primarily from the coverage of acid sites by carbonaceous species formed during reaction. After calcination in air, the coke is completely removed, restoring both catalytic performance (Fig. S31) and acidity (Fig. S30 and Table S4). This demonstrates that the acidity loss is due to reversible site blocking rather than framework degradation. As shown in Fig. S32, the H–Ni@Y catalyst experienced a gradual deactivation over 180 min on stream due to coke deposition. Crucially, the activity was fully recovered after a simple calcination step, demonstrating excellent regenerability. A benchmark comparison with reported heterogeneous catalysts (Fig. S33 and Table S6) confirms that H–Ni@Y excels in activity and 1-butene selectivity, while its stability is comparable but not superior. Furthermore, characterization of the regenerated catalyst (XRD, TEM) confirmed no changes in the zeolite topology or Ni dispersion, underscoring its robust structural integrity (Fig. S34 and S35).

Various zeolite samples incorporating different transition metals (H–M@Y, where M = Co, Ni, Cu, Zn) were examined for ethylene dimerization in the absence of cocatalysts (Fig. S36–S38). Among these, the H–Ni@Y catalyst distinctly stood out, underscoring nickel as the crucial active metal center necessary for efficient ethylene dimerization. Comparative experiments involving modified commercial Y zeolites (Fig. 4c and S39–S45) revealed negligible catalytic activity from purely acidic sites (H–Y), emphasizing the indispensable role of nickel active sites in driving the catalytic reaction. Ni–Y containing ion exchanged Ni species still exhibited limited performance, highlighting the importance of the specific coordination environment of Ni and acidity. Moreover, Ni-containing zeolites with varied acidity, such as H–Ni–Y and Ni–H–Y obtained by the traditional ion-exchange method, exhibited suboptimal catalytic activities and lower selectivity toward 1-butene, correlating well with results from Py-IR spectroscopy and NH_3-TPD analyses as previously mentioned. Further comparative assessments indicated that the H–Ni@Y catalyst outperformed previously reported benchmark Ni–Mg–Y catalysts in terms of activity,[19] as illustrated in Fig. 4d and Table S5. This enhanced performance is primarily attributed to the significantly improved Brønsted acidity of the H–Ni@Y catalyst. Consequently, the H–Ni@Y catalyst not only achieved outstanding ethylene dimerization activity and exceptional selectivity toward 1-butene without the need for additional cocatalysts, but also demonstrated substantial promise for developing innovative industrial catalytic processes.

2.3 Mechanistic investigation of ethylene dimerization

To elucidate the changes in the coordination environment of active nickel sites in the H–Ni@Y catalyst during ethylene dimerization, detailed X-ray absorption spectroscopy (XAS) analyses were performed (Fig. 5a and S46). The coordination number of nickel for the first coordination shell (Ni–O/C) notably increased from 3.8 to 4.2 upon exposure to ethylene (Table S3), indicating the gradual coordination of ethylene molecules to unsaturated nickel sites.

To further investigate the formation and evolution of surface species during ethylene dimerization, temperature-dependent *in situ* Fourier transform infrared spectroscopy (FTIR) was utilized. Analysis of H–Ni@Y exposed to ethylene (Fig. 5b) revealed distinct characteristic stretching bands appearing around 2877 cm^{-1}, assigned to the C–H stretching vibrations in $-CH_2$ groups of Ni–alkyl intermediates, and at approximately 2862 cm^{-1}, attributed to chemisorbed butene species.[7,25,32] These bands emerged at temperatures as low as 298 K, signifying rapid ethylene adsorption followed by efficient dimerization. Their intensities progressively increased with elevated temperature, reaching a maximum at 393 K, closely mirroring trends observed in the catalytic activity measurements (Fig. 4b). The rapid appearance and pronounced intensity of these spectral features directly correlate with the outstanding catalytic performance of H–Ni@Y. The deformation vibration of ethylene molecules chemically adsorbed to Ni species can be found at 1612 cm^{-1} and 1340 cm^{-1} belong to C=C stretching and C–H stretching adsorbed to the transition metal center, respectively,[33,34] confirming ethylene adsorption onto Ni active sites within H–Ni@Y (Fig. 5b). However, the infrared band ($\nu_{C=O}$ = 1710 cm^{-1}) of the hydroxyl group chemically adsorbed by ethylene molecules has not been found. Simultaneously, characteristic hydroxyl stretching vibrations were clearly detected, including bridging hydroxyl groups (Si–O(H)–Al) at 3603 cm^{-1},[35,36] isolated silanol (Si–OH) groups at 3732 cm^{-1},[37] and bridging hydroxyl groups within FAU zeolite supercages at 3653 cm^{-1}. These observations explicitly demonstrate the participation of the Brønsted acid sites during the reaction. Additionally, weaker overlapping bands at 3706, 3690, and 3642 cm^{-1} were attributed to Al–OH,[38] Ni–OH,[19] and additional Si–O(H)–Al functionalities,[39] respectively.

In stark contrast, Na–Ni@Y exhibited barely detectable absorption peaks around 2877 and 2860 cm^{-1}, even at elevated temperatures (393 K), consistent with its substantially inferior catalytic performance (Fig. S47). Similar underperformance was observed for the H–Ni–Y catalyst (Fig. S48). Furthermore, temperature-programmed surface reaction (TPSR) experiments (C_2H_4-TPSR, Fig. S49) provided direct evidence of ethylene-to-butene conversion, strongly aligning with the *in situ* FTIR results. Isotope labeling experiments using deuterated ethylene (C_2D_4-TPSR, Fig. S50) further revealed the formation of $C_4D_xH_{8-x}$ butene isotopologues, conclusively demonstrating the involvement of zeolite framework hydrogen species in ethylene dimerization and subsequent H–D exchange processes.

Time-dependent *in situ* FTIR analysis of H–Ni@Y exposure to C_2H_4 at 333 K (Fig. S51) was used to investigate the reaction rate. Firstly, the peaks attributed to Ni–alkyl motif (C–H stretching bands of CH_2 at 2875 cm^{-1}) and chemisorbed butene (C–H stretching bands of CH_3 at 2860 cm^{-1}) gradually emerged,[40] and the signal intensity increased over time. Subsequently, the infrared signal of hydroxyl group and gas phase (C_2H_4 and C_4H_8) infrared signal emerged, and their trend were consistent with the C–H stretching infrared signal as described above. These results underscored the superior catalytic performance of H–Ni@Y compared to Na–Ni@Y (Fig. S52). Moreover, the time-

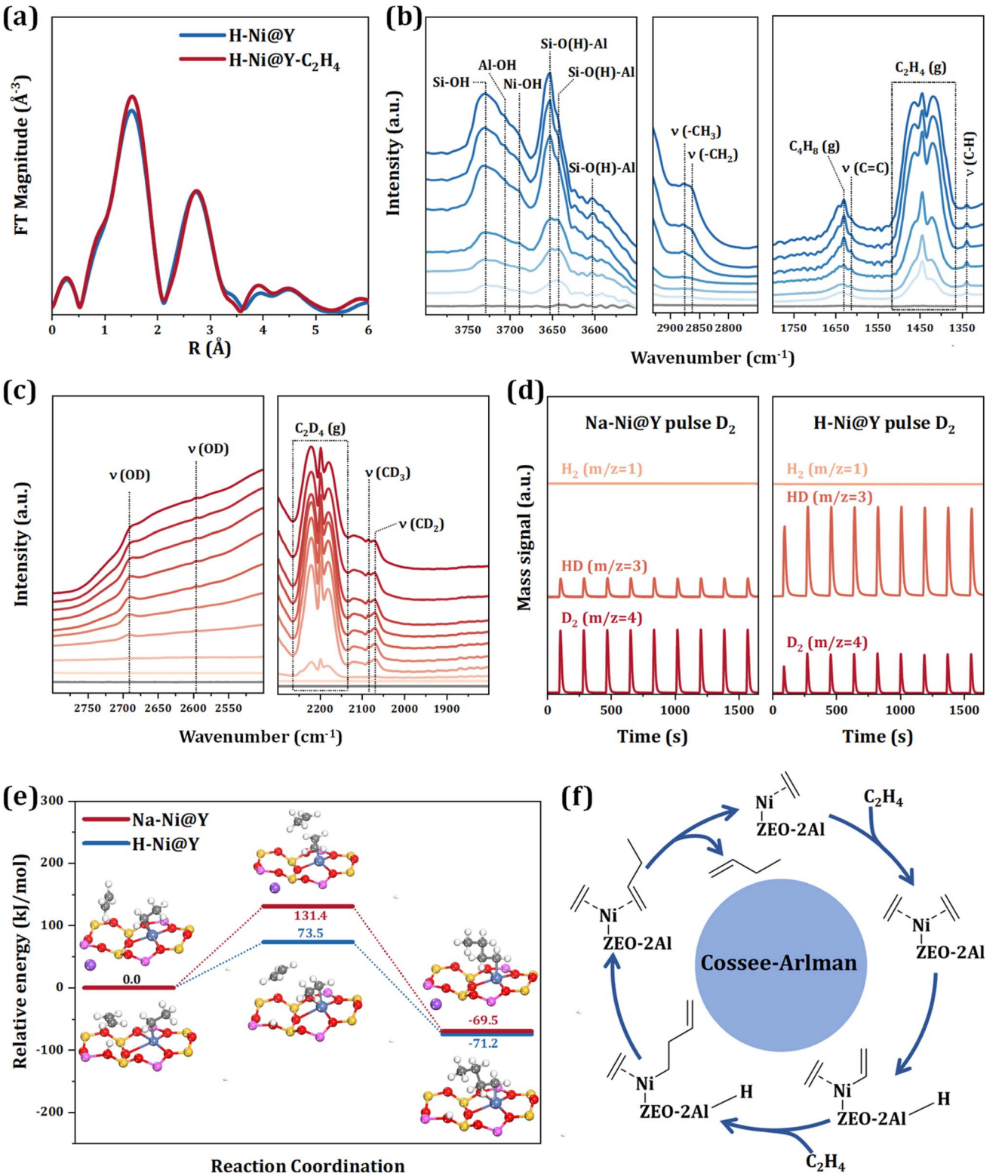

Fig. 5 Catalytic and reaction mechanism. (a) Changes of EXAFS when H–Ni@Y was exposed to ethylene under 333 K; the temperature-dependent *in situ* FTIR of (b) H–Ni@Y. Bottom to top: N_2, 298 K, 313 K, 333 K, 333 K, 353 K, 373 K, 393 K; (c) the time-dependent *in situ* FTIR of H–Ni@Y exposure to C_2D_4 under 333 K. Bottom to top: N_2, 1 min, 3 min, 5 min, 7 min, 10 min, 15 min, 20 min, 30 min, 40 min; (d) pulse-response experiments of feeding D_2 pulses to H–Ni@Y and Na–Ni@Y at 333 K; (e) free energy profiles of ethylene dimerization to butene over Na–Ni@Y and H–Ni@Y; (f) schematic illustration of the reaction mechanism of H–Ni@Y catalyst in ethylene dimerization, proposed as Cossee–Arlman pathway.

dependent *in situ* FTIR of H–Ni@Y exposure to C_2D_4 at 333 K (Fig. 5c) was further investigated. The adsorbed C_2D_4 at ~2200 cm^{-1} and CD_3 ($\nu_{C-D} = 2071$ cm^{-1}, $\nu_{C-H}/\nu_{C-D} \approx 1.38$) were appeared;[41,42] meanwhile, the hydroxy group (OD) of zeolite acid sites at 2688 and 2596 cm^{-1} ($\nu_{O-H}/\nu_{O-D} \approx 1.39$) were observed[43] only on H–Ni@Y catalyst rather than Na–Ni@Y (Fig. S53). That is, the abundant acidic sites in the H–Ni@Y catalyst promote the occurrence of ethylene dimerization by participating in the hydrogen transfer process. H–D exchange (Fig. 5d) and *in situ* FTIR results (Fig. 5) confirm that Brønsted sites are crucial for hydrogen transfer. To evaluate their role in desorption, 1-butene-TPD experiments were conducted on H–Ni@Y and Na–Ni@Y (Fig. S54). Both showed nearly identical desorption profiles, indicating that product desorption is primarily governed by Ni sites. Hence, Brønsted sites chiefly facilitate hydrogen transfer rather than product release. According to the density functional theory (DFT) calculations (Fig. 5e), the Brønsted acid site adjacent to the Ni-containing six-membered ring facilitated the formation of the Ni–buteryl species by immobilizing and activating ethylene at a much lower energy (73.5 kJ mol^{-1}) than that required for Na–Ni@Y (131.4 kJ mol^{-1}). These results confirmed that Brønsted acidic sites within the H–Ni@Y zeolite framework substantially promote proton transfer events, thereby significantly enhancing butene formation during ethylene dimerization.

Based on experimental evidence and DFT results, we proposed the following sequence: (i) coordinatively unsaturated Ni sites primarily adsorb and activate ethylene molecules. (ii) The formation of the key $C_2H_5^*$ intermediate requires synergy: Ni sites activate two ethylene molecules, while adjacent Brønsted acid sites facilitate C–C bond coupling *via* proton transfer. (iii) The final steps (hydrogen transfer and β-H elimination to yield 1-butene) are predominantly promoted by Brønsted acid sites. Thereby the reaction mechanism for ethylene dimerization over H–Ni@Y was proposed as Fig. 5f. *In situ* generated Ni–alkyl species represent the intrinsic active sites, with ethylene dimerization proceeding *via* the Cossee–Arlman pathway, facilitated by dynamic proton transfers. The zeolite framework and the precise positioning of Ni and acidic sites synergistically promote hydrogen transfer, enhancing catalytic performance in a manner analogous to cocatalysts in homogeneous systems. Consequently, the uniquely optimized structural and acidic configuration of H–Ni@Y constitutes an exceptionally effective catalyst platform for the selective ethylene dimerization to 1-butene.

3 Conclusions

In this study, a ligand-protected hydrothermal synthesis combined with NH_4^+ ion exchange was developed to produce H–Ni@Y zeolite with well-defined, coordinatively unsaturated Ni species and abundant Brønsted acid sites. The H–Ni@Y catalyst exhibited exceptional performance for ethylene dimerization, delivering high rates of 1-butene formation and remarkable selectivity in the absence of any additives. Comprehensive spectroscopic characterizations and density functional theory (DFT) calculations identified the *in situ* formed Ni–alkyl species as the intrinsic active sites, with ethylene dimerization proceeding *via* the Cossee–Arlman mechanism, facilitated by proton transfer processes. The findings presented here significantly advance the understanding of zeolite-catalyzed ethylene dimerization, highlighting the potential of Ni-confined zeolites as highly effective catalysts for this important industrial reaction.

Author contributions

L. W. conducted the sample synthesis, characterization and catalytic studies. Y. N. and J. Y. conducted the sample synthesis. G. W. analyzed the data and provided helpful discussions. Y. C. and L. L. directed and supervised the project. L. W., Y. C. and L. L. prepared the manuscript.

Conflicts of interest

There are no conflicts to declare.

Data availability

The authors declare that the data supporting the findings of this study are available within the manuscript and its supplementary information (SI). Should any raw data files be needed in another format they are available from the corresponding author (cyc@nankai.edu.cn) upon reasonable request. Source data are provided with this manuscript.

Supplementary information: preparation methods for samples, experimental procedures, and experimental data (XRD, TEM, XAS, FTIR, NH_3-TPD). See DOI: **https://doi.org/10.1039/d5sc05078b**.

Acknowledgements

This work was supported by the National Natural Science Foundation of China (22472077, 22025203), the China National Postdoctoral Program for Innovative Talents (BX20200171), and the Fundamental Research Funds for the Central Universities (Nankai University).

References

1 A. G. Popov, V. S. Pavlov and I. I. Ivanova, Effect of crystal size on butenes oligomerization over MFI catalysts, *J. Catal.*, 2016, **335**, 155–164.
2 J. Skupinska, Oligomerization of alpha-olefins to higher oligomers, *Chem. Rev.*, 1991, **91**, 613–648.
3 C. Chen, M. R. Alalouni, X. Dong, Z. Cao, Q. Cheng, L. Zheng, L. Meng, C. Guan, L. Liu, E. Abou-Hamad, J. Wang, Z. Shi, K. W. Huang, L. Cavallo and Y. Han, Highly Active Heterogeneous Catalyst for Ethylene Dimerization Prepared by Selectively Doping Ni on the Surface of a Zeolitic Imidazolate Framework, *J. Am. Chem. Soc.*, 2021, **143**, 7144–7153.

4 V. Hulea, Toward Platform Chemicals from Bio-Based Ethylene: Heterogeneous Catalysts and Processes, *ACS Catal.*, 2018, **8**, 3263–3279.
5 C. Wang, G. Li, Z. Huang and A. Peng, Ethylene Oligomerization into Linear α-Olefins Catalyzed by VSB-5 without Alkyl-Aluminum Cocatalysts, *Ind. Eng. Chem. Res.*, 2024, **63**, 13025–13036.
6 W. Chen, P. Elumalai, H. Mamlouk, Á. Rentería-Gómez, Y. Veeranna, S. Shetty, D. Kumar, M. m. Al-Rawashdeh, S. S. Gupta, O. Gutierrez, H. C. Zhou and S. T. Madrahimov, Monodentate Phosphinoamine Nickel Complex Supported on a Metal–Organic Framework for High-Performance Ethylene Dimerization, *Adv. Sci.*, 2024, **11**, 2309540.
7 E. D. Metzger, C. K. Brozek, R. J. Comito and M. Dinca, Selective Dimerization of Ethylene to 1-Butene with a Porous Catalyst, *ACS Cent. Sci.*, 2016, **2**, 148–153.
8 N. J. LiBretto, Y. Xu, A. Quigley, E. Edwards, R. Nargund, J. C. Vega-Vila, R. Caulkins, A. Saxena, R. Gounder, J. Greeley, G. Zhang and J. T. Miller, Olefin oligomerization by main group Ga^{3+} and Zn^{2+} single site catalysts on SiO_2, *Nat. Commun.*, 2021, **12**, 2322.
9 H. Olivier-Bourbigou, P. A. R. Breuil, L. Magna, T. Michel, M. F. Espada Pastor and D. Delcroix, Nickel Catalyzed Olefin Oligomerization and Dimerization, *Chem. Rev.*, 2020, **120**, 7919–7983.
10 T. Zanette, Y. M. Variani, B. P. Nicola, S. Gutiérrez-Tarriño, C. Cerezo-Navarrete, G. Agostini, P. Oña-Burgos, C. W. Lopes and K. Bernardo-Gusmão, Synthesis of NiZn-based paddle-wheel metal-organic framework and its use as a catalytic precursor for ethylene dimerization, *Catal. Today*, 2025, **444**, 114988.
11 T. Otroshchenko, D. I. Sharapa, E. A. Fedorova, D. Zhao and E. V. Kondratenko, Highly Efficient Low-loaded PdOx/AlSiOx Catalyst for Ethylene Dimerization, *Angew. Chem., Int. Ed.*, 2024, **63**, e202410646.
12 R. Diaz Arroyo, Y. G. Hur and R. Gounder, Influence of aluminum zoning toward external surfaces in MFI zeolites on propene oligomerization catalysis, *Dalton Trans.*, 2024, **53**, 12057–12063.
13 S. Wang, P. Wang, Z. Qin, Y. Chen, M. Dong, J. Li, K. Zhang, P. Liu, J. Wang and W. Fan, Relation of Catalytic Performance to the Aluminum Siting of Acidic Zeolites in the Conversion of Methanol to Olefins, Viewed via a Comparison between ZSM-5 and ZSM-11, *ACS Catal.*, 2018, **8**, 5485–5505.
14 H. Wang, F. Jiao, J. Feng, Y. Zhang, Z. Xu, X. Pan and X. Bao, Maximizing the Accessibility of Acid Sites Within Zeolite Catalysts for Syngas Conversion, *Angew. Chem., Int. Ed.*, 2025, e202424946.
15 Z. Pan, A. Puente-Urbina, S. R. Batool, A. Bodi, X. Wu, Z. Zhang, J. A. van Bokhoven and P. Hemberger, Tuning the zeolite acidity enables selectivity control by suppressing ketene formation in lignin catalytic pyrolysis, *Nat. Commun.*, 2023, **14**, 4512.
16 O. Abed, H. O. Mohamed, I. Hita, V. Velisoju, N. Morlanés, O. El Tall and P. Castaño, Ethylene Oligomerization: Unraveling the Roles of Ni Sites, Acid Sites, and Zeolite Pore Topology through Continuous and Pulsed Reactions, *ChemCatChem*, 2023, **16**, e202301220.
17 V. P. Ananikov, Nickel: The "Spirited Horse" of Transition Metal Catalysis, *ACS Catal.*, 2015, **5**, 1964–1971.
18 Z. N. Lashchinskaya, A. A. Gabrienko and A. G. Stepanov, Mechanisms of Light Alkene Oligomerization on Metal-Modified Zeolites, *ACS Catal.*, 2024, **14**, 4984–4998.
19 L. Wang, J. Ke, Y. Chai, G. Wu, C. Wang and L. Li, Additive-Free Ethylene Dimerization Over Well-Defined Nickel-Zeolite Catalysts, *Angew. Chem., Int. Ed.*, 2025, e202502563.
20 Q. Chen, P. Peng, G. Yang, Y. Li, M. Han, Y. Tan, C. Zhang, J. Chen, K. Jiang, L. Liu, C. Ye and E. Xing, Template-Guided Regioselective Encaging of Platinum Single Atoms into Y Zeolite: Enhanced Selectivity in Semihydrogenation and Resistance to Poisoning, *Angew. Chem., Int. Ed.*, 2022, **61**, e202205978.
21 X. Deng, R. Bai, Y. Chai, Z. Hu, N. Guan and L. Li, Homogeneous-like Alkyne Selective Hydrogenation Catalyzed by Cationic Nickel Confined in Zeolite, *CCS Chem.*, 2022, **4**, 949–962.
22 J. Yao, Y. He, Y. Zeng, X. Feng, J. Fan, S. Komiyama, X. Yong, W. Zhang, T. Zhao, Z. Guo, X. Peng, G. Yang and N. Tsubaki, Ammonia pools in zeolites for direct fabrication of catalytic centers, *Nat. Commun.*, 2022, **13**, 935.
23 Y. Guo, W. Tai, M. Zhao, X. Chen, Y. Chai, G. Wu and L. Li, Synthesis of self-pillared pentasil zeolites without organic templates and seeds, *Nanoscale*, 2024, **16**, 21594–21603.
24 W. Ding, D. Ji, K. Wang, Y. Li, Q. Luo, R. Wang, L. Li, X. Qin and S. Peng, Rapid Surface Reconstruction of Amorphous-Crystalline NiO for Industrial-Scale Electrocatalytic PET Upcycling, *Angew. Chem., Int. Ed.*, 2024, **64**, e202418640.
25 Y. Chai, G. Wu, X. Liu, Y. Ren, W. Dai, C. Wang, Z. Xie, N. Guan and L. Li, Acetylene-Selective Hydrogenation Catalyzed by Cationic Nickel Confined in Zeolite, *J. Am. Chem. Soc.*, 2019, **141**, 9920–9927.
26 J. Zheng, L. Löbbert, S. Chheda, N. Khetrapal, J. Schmid, C. A. Gaggioli, B. Yeh, R. Bermejo-Deval, R. K. Motkuri, M. Balasubramanian, J. L. Fulton, O. Y. Gutiérrez, J. I. Siepmann, M. Neurock, L. Gagliardi and J. A. Lercher, Metal-organic framework supported single-site nickel catalysts for butene dimerization, *J. Catal.*, 2022, **413**, 176–183.
27 H. Guesmi, D. Costa, D. Berthomieu and P. Massiani, Nickel Coordination to Lattice Oxygens in Basic LSX, X and Y Sodium Faujasites: A DFT Study, *J. Phys. Chem. C*, 2011, **115**, 5607–5618.
28 C. Chizallet, C. Bouchy, K. Larmier and G. Pirngruber, Molecular Views on Mechanisms of Brønsted Acid-Catalyzed Reactions in Zeolites, *Chem. Rev.*, 2023, **123**, 6107–6196.
29 R. Liu, Y. Bian and W. Dai, Qualitative and quantitative analysis of Brønsted and Lewis acid sites in zeolites: A combined probe-assisted ^1H MAS NMR and NH_3-TPD investigation, *Chin. J. Struct. Chem.*, 2024, **43**, 100250.
30 Y. Chu, B. Han, A. Zheng and F. Deng, Influence of Acid Strength and Confinement Effect on the Ethylene

Dimerization Reaction over Solid Acid Catalysts: A Theoretical Calculation Study, *J. Phys. Chem. C*, 2012, **116**, 12687–12695.

31 W. Shen, A theoretical study of confinement effect of zeolite on the ethylene dimerization reaction, *Microporous Mesoporous Mater.*, 2017, **247**, 136–144.

32 J. Liu, J. Wang, Y. Zhang, W. Zheng, Y. Yao, Q. Liu, X. Zhang, Y. Yang and X. Wang, Improved C–H Activation in Propane Dehydrogenation Using Zeolite-Stabilized Co–O Moieties, *ACS Catal.*, 2023, **13**, 14737–14745.

33 A. Ehrmaier, Y. Liu, S. Peitz, A. Jentys, Y.-H. C. Chin, M. Sanchez-Sanchez, R. Bermejo-Deval and J. Lercher, Dimerization of Linear Butenes on Zeolite-Supported Ni^{2+}, *ACS Catal.*, 2018, **9**, 315–324.

34 S. Moussa, P. Concepción, M. A. Arribas and A. Martínez, Nature of Active Nickel Sites and Initiation Mechanism for Ethylene Oligomerization on Heterogeneous Ni-beta Catalysts, *ACS Catal.*, 2018, **8**, 3903–3912.

35 I. Kiricsi, C. Flego, G. Pazzuconi, W. J. Parker, R. Millini, C. Perego and G. Bellussi, Progress toward Understanding Zeolite β Acidity: An IR and ^{27}Al NMR Spectroscopic Study, *J. Phys. Chem.*, 1994, **98**, 4627–4634.

36 Y. Nie, Y. Ma, J. Hu, X. Yang, L. Zhou and Y. Su, Synthesis of Al-containing Sn-beta with tunable brønsted and lewis acidity for conversion of glucose to 5-hydroxymethylfurfural, *Microporous Mesoporous Mater.*, 2024, **374**, 113157.

37 M. Guisnet, P. Ayrault, C. Coutanceau, M. F. Alvarez and J. Datka, Acid properties of dealuminated beta zeolites studied by IR spectroscopy, *J. Chem. Soc., Faraday Trans.*, 1997, **93**, 1661–1665.

38 C. Martinez-Macias, P. Xu, S.-J. Hwang, J. Lu, C.-Y. Chen, N. D. Browning and B. C. Gates, Iridium Complexes and Clusters in Dealuminated Zeolite HY: Distribution between Crystalline and Impurity Amorphous Regions, *ACS Catal.*, 2014, **4**, 2662–2666.

39 J. Datka, E. Broclawik, B. Gil and M. Sierka, O-H stretching frequencies in NaHX and NaHY zeolites: IR spectroscopic studies and quantum chemical calculations, *J. Chem. Soc., Faraday Trans.*, 1996, **92**, 4643–4646.

40 M. A. Artsiusheuski, R. Verel, J. A. van Bokhoven and V. L. Sushkevich, Selective Oxidative Dehydrogenation of Ethane and Propane over Copper-Containing Mordenite: Insights into Reaction Mechanism and Product Protection, *Angew. Chem., Int. Ed.*, 2023, **62**, e202309180.

41 E. Groppo, C. Lamberti, S. Bordiga, G. Spoto, A. Damin and A. Zecchina, FTIR Investigation of the H_2, N_2, and C_2H_4 Molecular Complexes Formed on the Cr(II) Sites in the Phillips Catalyst: a Preliminary Step in the understanding of a Complex System, *J. Phys. Chem. B*, 2005, **109**, 15024–15031.

42 K. Amakawa, S. Wrabetz, J. Kröhnert, G. Tzolova-Müller, R. Schlögl and A. Trunschke, In Situ Generation of Active Sites in Olefin Metathesis, *J. Am. Chem. Soc.*, 2012, **134**, 11462–11473.

43 A. J. Liang, R. Craciun, M. Chen, T. G. Kelly, P. W. Kletnieks, J. F. Haw, D. A. Dixon and B. C. Gates, Zeolite-Supported Organorhodium Fragments: Essentially Molecular Surface Chemistry Elucidated with Spectroscopy and Theory, *J. Am. Chem. Soc.*, 2009, **131**, 8460–8473.